Dimeric assembly of F_1-like ATPase for the gliding motility of *Mycoplasma*

Takuma Toyonaga[1,2], Takayuki Kato[3], Akihiro Kawamoto[3], Tomoko Miyata[4,5], Keisuke Kawakami[6], Junso Fujita[4,5,7], Tasuku Hamaguchi[8], Keiichi Namba[4,5], Makoto Miyata[1,2]

[1]Graduate School of Science, Osaka Metropolitan University, 3-3-138 Sugimoto, Sumiyoshi-ku, Osaka 558-8585, Japan

[2]The OMU Advanced Research Institute for Natural Science and Technology (OCARINA), Osaka Metropolitan University, 3-3-138 Sugimoto, Sumiyoshi-ku, Osaka 558-8585, Japan

[3]Institute for Protein Research, Osaka University, 3-2 Yamadaoka, Suita, Osaka 565-0871, Japan

[4]Graduate School of Frontier Biosciences, Osaka University, 1-3 Yamadaoka, Suita, Osaka 565-0871, Japan

[5]JEOL YOKOGUSHI Research Alliance Laboratories, Osaka University, 1-3 Yamadaoka, Suita, Osaka 565-0871, Japan

[6]Biostructual Mechanism Laboratory, RIKEN, SPring-8 Center, 1-1-1, Kouto, Sayo, Hyogo 679-5148, Japan

[7]Graduate School of Pharmaceutical Sciences, Osaka University, 1-6 Yamadaoka, Suita, Osaka 565-0871, Japan

[8]Institute of Multidisciplinary Research for Advanced Materials, Tohoku University, 2-

1-1 Katahira, Aoba-ku, Sendai 980-8577, Japan

Corresponding author: Makoto Miyata; Email: miyata@omu.ac.jp

Present address: Takuma Toyonaga: Institute of Multidisciplinary Research for Advanced Materials, Tohoku University, 2-1-1 Katahira, Aoba-ku, Sendai 980-8577, Japan

Abstract

Rotary ATPases, including F_1F_o- and V/A-ATPases, are molecular motors that exhibit rotational movements for energy conversion[1]. In the gliding bacterium, *Mycoplasma mobile*, a dimeric F_1-like ATPase forms a chain structure with the glycolytic enzyme, phosphoglycerate kinase (PGK), within the cell[2], which is proposed to drive the bacterial gliding motility[2–4]. However, the mechanisms of force generation and transmission remain unclear. Here, we present a 3.2 Å resolution structure of the dimeric ATPase complex obtained using electron cryomicroscopy (cryo-EM). Notably, the structure revealed an assembly distinct from that of known dimeric forms of F_1F_o-ATPase[5], despite containing conserved F_1-ATPase structures. The two ATPase units were interconnected by GliD dimers, previously identified as MMOB1620[2,6]. Gliβ, a homologue of the F_1-ATPase catalytic subunit[6], exhibited a specific N-terminal region that incorporates PGK into the complex. Structural conformations of the catalytic subunits, catalytically important residues, and nucleotide-binding pattern of the catalytic sites of the ATPase displayed strong similarities to F_1-ATPase, suggesting a rotation based on the rotary catalytic mechanism conserved in rotary ATPases[1,7–10]. Overall, the

48 cryo-EM structure underscores an evolutionary connection in the rotary ATPases and
49 provides insights into the mechanism through which F_1-like ATPase drives bacterial
50 gliding motility.
51

52 **Introduction**

53 Rotary ATPases are molecular motors that link ATP hydrolysis or synthesis with ion
54 transport via rotational motion in biological membranes[1]. These motors comprise two
55 common domains: soluble R_1, which is responsible for ATP hydrolysis and synthesis,
56 and membrane-embedded R_o, which is responsible for ion transport. F_1F_o-ATPase, one
57 of the rotary ATPases conserved across most eukaryotes, archaea, and bacteria, is
58 responsible for ATP synthesis and the maintenance of membrane potential[5]. An F_1-like
59 ATPase gene cluster, referred to as Type 2 ATPase, was reported in four *Mycoplasma*
60 species, *M. mobile*, *M. pulmonis*, *M. agassizii*, and *M. testudineum*, in addition to the
61 genuine F_1F_o-ATPase gene cluster, referred to as Type 1 ATPase[11,12] (Extended Data Fig.
62 1). The presence of F_1-ATPase α and β subunit homologues (MMOBs 1660 and 1670 in
63 *M. mobile*) in the Type 2 ATPase gene cluster suggests a shared evolutionary origin in
64 the F_1 domain. Type 2 ATPase is proposed to drive the gliding motility observed in *M.*
65 *mobile* and *M. pulmonis*[2–4,13,14]. *M. mobile*, a fish pathogen, glides at speeds of up to 4
66 μm per second on a solid surface covered with sialylated oligosaccharides found on host
67 cell surfaces[15] (Fig. 1a, Extended Data Fig. 2). In our proposed model for gliding,
68 filamentous leg structures on the mycoplasma cell surface, which are approximately 50
69 nm, propel the cell body by catching and pulling sialylated oligosaccharides on the solid
70 surface. Inside the cell, motors composed of Type 2 ATPase and phosphoglycerate
71 kinase (PGK), which converts ADP to ATP through glycolysis, are linked near the cell

72 membrane to form 'internal chains'[2,6]. The motor is formed by dimerised F_1-like
73 ATPase units with unique bridge structures and is referred to as a twin motor. However,
74 the mechanisms of force generation and transmission remain unclear. This study aimed
75 to elucidate the detailed structure of the twin motor using cryo-EM single-particle
76 analysis (SPA). Notably, the structural features had a strong homology to those of F_1-
77 ATPase[7,8], suggesting a rotary catalytic mechanism analogous to that of rotary
78 ATPase[1,9,10] for the gliding motility of *M. mobile*.
79

80 **Results**

81 **Protein identification using the cryo-EM structure of twin motor**

82 Cryo-EM SPA was performed for twin motors isolated from *M. mobile* cells using
83 images collected on the epoxidised graphene grid (EG-grid)[16] (Extended Data Table 1).
84 The overall 3D structure of the twin motor was determined at a resolution of 3.2 Å (Fig.
85 1b, Extended Data Figs. 3, 4). Local refinement improved the resolution of the regions,
86 each containing the F_1-like ATPase unit, to 3.1 Å (Extended Data Figs. 3b, 4). The
87 density maps enabled the construction of the atomic model of the twin motor (Fig. 1c).
88 The modelled sequence regions of each subunit are summarised in Extended Data Table
89 2. The twin motor exhibited a rectangular structure with dimensions of approximately
90 350 × 250 × 150 Å and at least 24 polypeptide chains with a total mass of
91 approximately 1.5 MDa. Notably, the two F_1-like ATPase units were inclined to each
92 other by approximately 5° and formed a dimer with pseudo-two-fold rotational
93 symmetry and several accessories (Fig. 1c, d). The F_1-like ATPase comprised a
94 hexameric ring of two alternating subunits and a central shaft subunit, identified as
95 MMOBs 1660, 1670, and 1630, respectively. In the present study, these subunits were

named Gliα, Gliβ, and Gliγ, according to the subunit names of F_1-ATPase[10]. In the hexameric ring, nucleotide-derived densities were observed at five of the six subunit interfaces, despite the isolation and analysis of samples under nucleotide free condition, indicating the presence of endogenous nucleotides as reported in F_1-ATPase[17] (Fig. 1c, e). The subunit attached to Gliα, forming a 'bridge' between two F_1-like ATPase units, was identified as MMOB1620 and named GliD in the present study (Fig. 1c). The three densities protruding from the dimeric F_1-like ATPase were identified as MMOB4530, which was previously annotated as PGK. The denoised 3D map revealed additional distinct densities at six locations, including the $PGK_{1–3}$ regions (Extended Data Fig. 5a). These six densities exhibited correlation coefficients ranging from 0.37 to 0.48 with the crystal structure of PGK from *Staphylococcus aureus* (PDB ID: 4DG5) (Extended Data Fig. 5b, c). Although the values are low, these assignments are consistent with the stoichiometry previously estimated via SDS-PAGE[2], suggesting these maps are PGK molecules. A density bound only to one of the two F_1-like ATPase units was identified as MMOB3660, which was newly detected via SDS-PAGE of the twin motor and named GliE in the present study (Fig. 1b, c, Extended Data Fig. 6). This small protein (112 aa), characterised by a β-sandwich, was nestled between the ATPase hexamer and other subunits, breaking the rotational symmetry of the complex (Extended Data Fig. 7). Although MMOB1640, encoded in the Type 2 ATPase gene cluster, was detected via SDS-PAGE of the twin motor (Extended Data Fig. 6), the protein density was not observed from the overall 3D map.

Structural features of subunits comprising F_1-like ATPase

Gliβ and Gliα exhibited high structural similarity to the β and α subunits of the F_1-

120 ATPase from the thermophilic bacterium, *Bacillus* PS3[8] (PDB ID: 8HH5), based on the
121 superimposition of their Cα atoms with the root mean squared deviation (RMSD) values
122 of 1.95 Å and 2.79 Å, respectively (Fig. 1g, i). Both Gliβ and Gliα had three domains:
123 crown, nucleotide-binding domain (NBD), and C-terminal domain (CTD). The NBDs of
124 Gliβ and Gliα comprise a phosphate-binding motif of P-loop[18], consisting of the amino
125 acid sequences GGAGVGKT and GDRGTGKT, respectively (Fig. 1f, h). The Gliβ-
126 CTD contained a DELSEED loop, which is important for torque transmission in the F_1-
127 ATPase β subunit[19], with an amino acid sequence of DALSEDD (Fig. 1f). A remarkable
128 difference between Gliβ and the F_1-ATPase β subunit was the presence of an extended
129 N-terminal region consisting of the N-terminal domain (NTD) and linker (Fig. 1f,
130 Extended Data Fig. 8a). This region comprised approximately 100 residues located
131 within the extra N-terminal 299 residues of Gliβ[6,12]. Notably, the linker hangs outside
132 the F_1-like ATPase along the crown and NBD (Extended Data Fig. 8b). Gliβ-NTDs,
133 consisting of 4 to 6 helices, were oriented in various directions among Gliβ, depending
134 on their position in the complex (Extended Data Fig. 8a, c, d). Further, Gliβ-NTD
135 interacted with PGK (Fig. 2a, b). In addition, at the interface of the two F_1-like ATPase
136 units, the N-terminal regions of $Gli\beta_3$ and $Gli\beta_6$ interacted with the NBDs of $Gli\alpha_6$ and
137 $Gli\alpha_3$ of another F_1-like ATPase unit, respectively (Fig. 2a, c). These interactions
138 suggest that the Gliβ-specific N-terminal region plays a role in the incorporation of
139 PGK into the twin motor and stabilisation of the ATPase dimer. A difference between
140 Gliα and the F_1-ATPase α subunit is the absence of the H1 helix, which interacts with
141 the peripheral stalk[20] (Extended Data Fig. 9). This absence is consistent with the lack of
142 a gene homologous to the peripheral stalk in the Type 2 ATPase gene cluster[12]. Gliγ,
143 which is composed of a coiled coil and an α/β fold typical of the F_1-ATPase γ subunit,

144 was superimposed on the γ subunit of the *Bacillus* PS3 F_1-ATPase with an RMSD value
145 of 5.79 Å for Cα atoms due to a lower sequence conservation than that of the catalytic
146 subunits[15] (Fig. 1j, k). The folded C-terminal α-helix, which is 25 Å longer than the F_1-
147 ATPase γ subunit, protrudes from the N-terminal side of the hexameric ring and
148 interacts with the crowns of Gliαβ (Fig. 1k, Extended Data Fig. 10a, b). The coiled coil
149 of Gliγ hydrophobically interacted with the CTDs of Gliαβ in the hexameric ring
150 (Extended Data Fig. 10c), and in the F_1-ATPase, this interaction is involved in axle hold
151 and torque transmission[21].
152
153 **Accessories of dimeric F_1-like ATPase**
154 Generally, PGK is bifurcated into two domains interconnected by an α-helix: the NTD,
155 which binds to 3-phosphoglycerate (3-PG) or 1,3-bisphosphoglycerate (1,3-BPG), and
156 the CTD, which binds to Mg-ADP or Mg-ATP[22] (Extended Data Fig. 11a). The twin-
157 motor PGK structure, comprising the CTD and a segment of the α-helix, exhibited a
158 high structural similarity to the PGK from *S. aureus* (PDB ID: 4DG5), with an RMSD
159 value of 3.12 Å for Cα atoms (Extended Data Fig. 11b, c). The β loop of the PGK-CTD
160 invades the depression of the folded Gliβ-NTD and interacts with the H2 helix and the
161 H2–H3 loop of the Gliβ-NTD (Fig. 2d). The H4–β loop and H5 helix of the PGK-CTD
162 also interacted with the H5 and H4 helices of the Gliβ-NTD, respectively. Nucleotide-
163 derived densities were not found in the PGK-CTD of the twin motor, despite
164 conservation of the residues important for nucleotide binding in PGK[23] (Extended Data
165 Figs. 11d–f, 12). None of the twin-motor PGK-NTDs were modelled due to the poor
166 densities of the reconstruction. However, the binding and catalytic residues for 3-PG or
167 1,3-BPG in PGK were conserved in terms of amino acid sequence, suggesting that the

168 twin-motor PGK possesses enzymatic activity (Extended Data Fig. 12). As the binding
169 and catalytic residues were not conserved in another PGK homologue, MMOB4490,
170 encoded in the *M. mobile* genome, the twin-motor PGK is expected to function as the
171 original PGK in glycolysis (Extended Data Fig. 12). The GliD ($GliD_{1,3,4,6}$) bridge
172 components formed dimers at the interface of two F_1-like ATPase units, whereas $GliD_{2,5}$
173 at the twin-motor end existed as monomers (Fig. 2a, e, f). GliD contained a globular
174 domain and an N-terminal long α-helix (H2), which was only visualised in the dimer.
175 The globular domain interacted with the H20–H25 region at the C-terminus of Gliα
176 (Fig. 2g, h). The two H2 helices in the GliD dimer aligned parallel to each other across
177 the H20–H25 region of Gliα, GliE, Gliβ-NTD, and Gliβ-CTD (Fig. 2f). These two α-
178 helices are reminiscent of the dynein buttress that connects the AAA+ ring and the
179 tubulin-binding domain[24], suggesting a regulatory role for structural changes induced by
180 the ATPase activity of the F_1-like ATPase units.
181

182 **Structural information suggesting a catalytic mechanism analogous to that of F_1-**
183 **ATPase**

184 The crown region of the hexameric ring exhibited approximately six-fold rotational
185 symmetry, whereas the CTD region was asymmetric (Extended Data Fig. 10a). This
186 observation suggests a structural change with a pivot point between the crown and
187 CTD. $Gli\beta_{1–3}$ adopted three distinct conformations, which appear to be the transition
188 states of CTD flexion motion towards Gliγ, with a positional difference of 11 Å for the
189 DELSEED loop (Fig. 3a). These conformations were named $Gli\beta_C$ (closed), $Gli\beta_{HO}$
190 (half-open), and $Gli\beta_O$ (open), according to the conformation names of F_1-ATPase[8]. The
191 conformations were arranged clockwise when viewed from the C-terminus of the

192 hexameric ring (Fig. 3b). These conformations resemble the states referred to as *ATP-*
193 *waiting* or *step-waiting*, which occurs during the catalytic reaction of *Bacillus* PS3 F_1-
194 ATPase; the latter occurs after ATP binding[8] (Extended Data Table 3). In Gliα, the
195 region corresponding to the DELSEED loop exhibited only a 5 Å difference in position
196 relative to the Gliγ side, whereas the H20–H25 region interacting with GliD exhibited a
197 difference of 9 Å (Extended Data Fig. 13). These conformations were named $Gli\alpha_C$
198 (close), $Gli\alpha_{HO}$ (half-open), and $Gli\alpha_O$ (open) based on the H20–H25 positions viewed
199 from the Gliγ side. If this difference in Gliα represents a conformational change
200 associated with ATP hydrolysis of the twin motor, force transfer may occur from F_1-like
201 ATPase to GliD. The catalytic sites formed at the α–β interface of $Gli\alpha_C\beta_C$ and
202 $Gli\alpha_{HO}\beta_{HO}$ contained Mg-ATP and Mg-ADP + P_i, respectively, whereas no nucleotide
203 density was found at the catalytic site of $Gli\alpha_O\beta_O$ (Fig. 3b–d, Extended Data Fig. 14).
204 The nucleotide-binding states were also shared between the two F_1-like ATPases
205 according to the pseudo-two-fold rotational symmetry. The residues of F_1-ATPase
206 involved in ATP hydrolysis, including those in the arginine finger, were conserved in
207 Gliαβ, suggesting a shared ATP hydrolysis pathway between F_1-ATPase and the twin
208 motor (Fig. 3d). Mg-ATP was observed at the remaining three interfaces, hereafter
209 referred to as the β–α interfaces (Fig. 3b, Extended Data Fig. 14). At the β–α interface,
210 Gliα-K179 corresponded to the position of conserved residue Q200 of the F_1-ATPase α
211 subunit (Extended Data Fig. 15a, b). Compared with the α–β interface, Gliα-K179 is
212 charge inverted relative to the glutamate essential for the catalytic activity (E190 of the
213 F_1-ATPase β subunit), suggesting that the β–α interface, akin to F_1-ATPase, does not
214 exhibit ATP hydrolysis activity (Extended Data Fig. 15c). The conformational sequence
215 pattern of three Gliβ subunits with bound nucleotides was identical to that of the *ATP-*

216 *waiting* state of F_1-ATPase[8] (Fig. 3b). These data suggest that Mg-ATP binding to the
217 catalytic site of Gli$\alpha_O\beta_O$ promotes the catalytic reaction of the entire F_1-like ATPase
218 based on the catalytic mechanism analogous to that of F_1-ATPase.
219
220 **Twin motors in the chain**
221 The atomic model of the twin motor was fitted into the previously reconstructed density
222 of the internal chain, obtained using negative staining electron microscopy (EM) SPA[2]
223 (Fig. 4a). To circumvent misfitting of the long-axis orientation of the twin motors due to
224 the low-resolution density map (29.7 Å) of the chain structure, regions with asymmetric
225 structures, such as the NTDs of Gli$\beta_{3,6}$, GliE, and PGK_3, were excluded from the fitted
226 model. At the interface between twin-motor units, GliDs that project along the long axis
227 of the twin motor faced each other, suggesting their role as a linker for chain formation.
228 However, the 3D map of the internal chain revealed a remaining density at the interface
229 that cannot be filled by GliDs, which may correspond to the approximately 100 residues
230 comprising an N-terminal region and loops that have not been modelled.
231
232 **Discussion**
233 The major difference between the twin motor and the dimeric form of eukaryotic
234 mitochondrial ATP synthases[5] is the interaction between the F_1 domains through GliD
235 and the N-terminal region of Gliβ. Although the GliD dimer does not have a
236 transmembrane segment, the two long α-helices at the N-terminus are reminiscent of the
237 structure of a peripheral stalk. This observation is consistent with the hypothesis that the
238 MMOB1620 gene encoding GliD is derived through gene fusion from the b and δ
239 subunits, which comprise the peripheral stalk[15]. The GliD-mediated dimer and chain

240 formation may allow F_1-like ATPase units to work cooperatively. Consistently, changes
241 in the distance between twin motors have been associated with the ATP hydrolysis
242 reaction, suggesting force transfer between the twin motors through GliD[3,4]. The PGK
243 in the twin motor may efficiently supply ATP to the ATPase as fuel. Further, PGK
244 molecules protruding from the transverse axis of the twin motor may be involved in the
245 sheet formation of the internal chain, according to negative staining EM[25]. The weak
246 density of PGK in the cryo-EM map can be explained by its flexibility, which was
247 identified using high-speed atomic force microscopy[2]. The flexibility of the PGK
248 molecule may suggest that the chain sheet serves as a cytoskeleton to withstand
249 mechanical stress in the mycoplasma cell, which does not have a cell wall. The GliE
250 subunit, which is bound to only one side of the dimeric F_1-like ATPase, creates
251 asymmetry in the twin motor structure and may contribute to the unidirectional nature
252 of the gliding motility. However, this protein may also bind to another side of the
253 dimeric F_1-like ATPase in the cell but dislodge during purification.
254 The three distinct forms of the catalytic subunit Gliβ and their corresponding nucleotide
255 binding suggest a rotary catalytic mechanism analogous to that of the rotary ATPases
256 (Fig. 4b). In this rotary catalytic mechanism, $Gli\alpha_O\beta_O$ transitions to $Gli\alpha_C\beta_C$, and the
257 DELSEED loop of Gliβ in this transition approaches Gliγ upon ATP binding at the
258 catalytic site. The other Gliαβ dimers in the hexameric ring also operate cooperatively,
259 with $Gli\alpha_C\beta_C$ transitioning to $Gli\alpha_{HO}\beta_{HO}$ upon ATP hydrolysis and $Gli\alpha_{HO}\beta_{HO}$
260 transitioning to $Gli\alpha_O\beta_O$ upon ADP and phosphate release. This one-step conformational
261 change of the hexameric ring prompts a 120° rotation of Gliγ. Each Gliαβ dimer
262 sequentially hydrolyses ATP, and through a three-step process, the hexameric ring
263 structure and position of Gliγ revert to their initial states. The pseudo-two-fold

264 rotational symmetry structure of the twin motor suggests that the two F_1-like ATPase
265 units operate in a synchronised manner, maintaining the structural symmetry.
266 Throughout the catalytic reaction, significant changes in the positioning of the two F_1-
267 like ATPase units within the twin motor may be hindered due to the presence of the N-
268 terminal regions of Gliβ bridging the two units and a buttress-like structure composed of
269 two long α-helices of the GliD dimer (Fig. 2a, c, f).
270 For cell gliding, the rotary motions of the twin motors must be converted into a linear
271 motion. This conversion mechanism may occur due to the membrane protein Gli521,
272 which consists of a hook and rod, thereby functioning as a crank[26] (Fig. 4c). Upon the
273 conversion of the rotary motion to linear motion, Gli521 pulls the leg protein, Gli349,
274 which is bound to sialylated oligosaccharides on the host cell surface, thereby propelling
275 the mycoplasma cell forward[27]. The presence of a globular domain in Gliγ, similar to
276 that in the F_1-ATPase γ subunit, suggests a potential interaction with a membrane-
277 embedded F_o-like domain. MMOB1610 and MMOB1650, encoded in the Type 2
278 ATPase gene cluster, possess 12 and 2 transmembrane segments, respectively[15]. These
279 two proteins are potential interaction partners for the globular domain of Gliγ at the cell
280 membrane, transmitting the rotary motion to Gli521 on the cell surface.
281 The roles of rotary ATPases and their relatives, such as the flagellar type III protein
282 export apparatus, which exhibit a hexameric ring with a central shaft, involve protein
283 and ion transport[28,29]. We hypothesised that F_1F_o-ATPase has acquired the role and
284 mechanism of the twin motor through an incidental contact with an adhesin on the
285 membrane during the evolution of mycoplasma from a non-motile to a motile state[2,30].
286 This primitive gliding motility would have conferred a survival advantage. Another F_1-
287 like ATPase, referred to as Type 3 ATPase, is also found in mycoplasma, and this F_1-like

288 ATPase may drive the system that cleaves host antibodies[12,31]. Notably, Type 2 and 3
289 ATPases transition from F_1-ATPase to drive mycoplasma-specific systems.
290 Understanding these unique F_1-like ATPases will contribute to investigations into the
291 working principles and evolution of rotary ATPases.
292

293 **References**

294 1. Stewart, A. G., Sobti, M., Harvey, R. P. & Stock, D. Rotary ATPases.
295 *Bioarchitecture* **3**, 2–12 (2013).
296 2. Toyonaga, T. *et al.* Chained structure of dimeric F1-like ATPase in *Mycoplasma*
297 *mobile* gliding machinery. *mBio* **12**, e0141421 (2021).
298 3. Nishikawa, M. S. *et al.* Refined mechanism of *Mycoplasma mobile* gliding based
299 on structure, ATPase activity, and sialic acid binding of machinery. *mBio* **10**,
300 e02846-19 (2019).
301 4. Kobayashi, K. *et al.* Movements of *Mycoplasma mobile* gliding machinery
302 detected by high-speed atomic force microscopy. *mBio* **12**, e0004021 (2021).
303 5. Kühlbrandt, W. Structure and mechanisms of F-Type ATP synthases. *Annu Rev*
304 *Biochem* **88**, 515–549 (2019).
305 6. Nakane, D. & Miyata, M. Cytoskeletal 'jellyfish' structure of *Mycoplasma mobile*.
306 *Proc Natl Acad Sci U S A* **104**, 19518–19523 (2007).
307 7. Noji, H. & Ueno, H. How Does F1-ATPase Generate Torque?: Analysis From
308 Cryo-Electron Microscopy and Rotational Catalysis of Thermophilic F1. *Front*
309 *Microbiol* **13**, 904084 (2022).
310 8. Nakano, A., Kishikawa, J. ichi, Mitsuoka, K. & Yokoyama, K. Mechanism of ATP
311 hydrolysis dependent rotation of bacterial ATP synthase. *Nat Commun* **14**, 4090

(2023).

9. Noji, H., Yasuda, R., Yoshida, M. & Kinosita, K. Direct observation of the rotation of F1-ATPase. *Nature* **386**, 299–302 (1997).

10. Abrahams, J. P., Leslie, A. G. W., Lutter, R. & Walker, J. E. Structure at 2.8 Å resolution of F1-ATPase from bovine heart mitochondria. *Nature* **370**, 621–628 (1994).

11. Tulum, I., Kimura, K. & Miyata, M. Identification and sequence analyses of the gliding machinery proteins from *Mycoplasma mobile*. *Scientific Reports 2020 10:1* **10**, 1–11 (2020).

12. Béven, L. *et al.* Specific evolution of F1-like ATPases in mycoplasmas. *PLoS One* **7**, e38793 (2012).

13. Bredt, W. & Radestock, U. Gliding motility of *Mycoplasma pulmonis*. *J Bacteriol* **130**, 937 (1977).

14. Rosengarten, R. & Kirchhoff, H. Gliding motility of Mycoplasma sp. nov. strain 163K. *J Bacteriol* **169**, 1891–1898 (1987).

15. Miyata, M. & Hamaguchi, T. Prospects for the gliding mechanism of *Mycoplasma mobile*. *Curr Opin Microbiol* **29**, 15–21 (2016).

16. Fujita, J. *et al.* Epoxidized graphene grid for highly efficient high-resolution cryoEM structural analysis. *Sci Rep* **13**, 2279 (2023).

17. Leimgruber, R. M. & Senior, A. E. Removal of 'tightly bound' nucleotides from phosphorylating submitochondrial particles. *Journal of Biological Chemistry* **251**, 7110–7113 (1976).

18. Menz, R. I., Walker, J. E. & Leslie, A. G. W. Structure of bovine mitochondrial F(1)-ATPase with nucleotide bound to all three catalytic sites: implications for the

336 mechanism of rotary catalysis. *Cell* **106**, 331–341 (2001).

337 19. Tanigawara, M. *et al.* Role of the DELSEED Loop in Torque Transmission of F1-
338 ATPase. *Biophys J* **103**, 970–978 (2012).

339 20. Sobti, M. *et al.* Cryo-EM structures of the autoinhibited *E. coli* ATP synthase in
340 three rotational states. *Elife* **5**, e21598 (2016).

341 21. Kohori, A. *et al.* Torque generation in F1-ATPase devoid of the entire amino-
342 terminal helix of the rotor that fills half of the stator orifice. *Biophys J* **101**, 188–
343 195 (2011).

344 22. Bowler, M. W. Conformational dynamics in phosphoglycerate kinase, an open and
345 shut case? *FEBS Lett* **587**, 1878–1883 (2013).

346 23. Rojas-Pirela, M. *et al.* Phosphoglycerate kinase: structural aspects and functions,
347 with special emphasis on the enzyme from Kinetoplastea. *Open Biol* **10**, 200302
348 (2020).

349 24. Rao, L., Berger, F., Nicholas, M. P. & Gennerich, A. Molecular mechanism of
350 cytoplasmic dynein tension sensing. *Nature Communications 2019 10:1* **10**, 1–17
351 (2019).

352 25. Fukushima, M., Toyonaga, T., Tahara, Y. O., Nakane, D. & Miyata, M. Internal
353 structure of *Mycoplasma mobile* gliding machinery analyzed by negative staining
354 electron tomography. *Biophys Physicobiol* e210015 (2024).

355 26. Nonaka, T., Adan-Kubo, J. & Miyata, M. Triskelion structure of the Gli521 protein,
356 involved in the gliding mechanism of *Mycoplasma mobile*. *J Bacteriol* **192**, 636–
357 642 (2010).

358 27. Hamaguchi, T., Kawakami, M., Furukawa, H. & Miyata, M. Identification of novel
359 protein domain for sialyloligosaccharide binding essential to *Mycoplasma mobile*

360 gliding. *FEMS Microbiol Lett* **366**, fnz016 (2019).

361 28. Ibuki, T. *et al.* Common architecture of the flagellar type III protein export
362 apparatus and F- and V-type ATPases. *Nat Struct Mol Biol* **18**, 277–282 (2011).

363 29. Majewski, D. D. *et al.* Cryo-EM structure of the homohexameric T3SS ATPase-
364 central stalk complex reveals rotary ATPase-like asymmetry. *Nat Commun* **10**, 626
365 (2019).

366 30. Miyata, M. *et al.* Tree of motility - A proposed history of motility systems in the
367 tree of life. *Genes. Cell* **25**, 6–21 (2020).

368 31. Nottelet, P. *et al.* The mycoplasma surface proteins MIB and MIP promote the
369 dissociation of the antibody-antigen interaction. *Sci Adv* **7**, eabf2403 (2021).

370 32. Aluotto, B. B., Wittler, R., Williams, C. & Faber, J. Standardized bacteriologic
371 techniques for the characterization of Mycoplasma species1, 2. *Int J Syst Evol*
372 *Microbiol* **20**, 35–58 (1970).

373 33. Miyata, M. *et al.* Gliding mutants of *Mycoplasma mobile*: relationships between
374 motility and cell morphology, cell adhesion and microcolony formation.
375 *Microbiology (Reading)* **146 (Pt 6)**, 1311–1320 (2000).

376 34. Uenoyama, A., Seto, S., Nakane, D. & Miyata, M. Regions on Gli349 and Gli521
377 protein molecules directly involved in movements of *Mycoplasma mobile* gliding
378 machinery, suggested by use of inhibitory antibodies and mutants. *J Bacteriol* **191**,
379 1982–1985 (2009).

380 35. Mizutani, M., Tulum, I., Kinosita, Y., Nishizaka, T. & Miyata, M. Detailed analyses
381 of stall force generation in *Mycoplasma mobile* gliding. *Biophys J* **114**, 1411–1419
382 (2018).

383 36. Hellman, U., Wernstedt, C., Góñez, J. & Heldin, C. H. Improvement of an 'In-Gel'

384 digestion procedure for the micropreparation of internal protein fragments for
385 amino acid sequencing. *Anal Biochem* **224**, 451–455 (1995).
386 37. Fujita, J. *et al.* Structures of a FtsZ single protofilament and a double-helical tube
387 in complex with a monobody. *Nat Commun* **14**, 4073 (2023).
388 38. Mastronarde, D. N. Automated electron microscope tomography using robust
389 prediction of specimen movements. *J Struct Biol* **152**, 36–51 (2005).
390 39. Punjani, A., Rubinstein, J. L., Fleet, D. J. & Brubaker, M. A. cryoSPARC:
391 algorithms for rapid unsupervised cryo-EM structure determination. *Nat Methods*
392 **14**, 290–296 (2017).
393 40. Zivanov, J. *et al.* A Bayesian approach to single-particle electron cryo-tomography
394 in RELION-4.0. *Elife* **11**, e83724 (2022).
395 41. Bepler, T., Kelley, K., Noble, A. J. & Berger, B. Topaz-Denoise: general deep
396 denoising models for cryoEM and cryoET. *Nat Commun* **11**, 5208 (2020).
397 42. Jumper, J. *et al.* Highly accurate protein structure prediction with AlphaFold.
398 *Nature* **596**, 583–589 (2021).
399 43. Šali, A. & Blundell, T. L. Comparative protein modelling by satisfaction of spatial
400 restraints. *J Mol Biol* **234**, 779–815 (1993).
401 44. Pettersen, E. F. *et al.* UCSF Chimera--a visualization system for exploratory
402 research and analysis. *J Comput Chem* **25**, 1605–1612 (2004).
403 45. Emsley, P., Lohkamp, B., Scott, W. G. & Cowtan, K. Features and development of
404 Coot. *Acta Crystallogr D Biol Crystallogr* **66**, 486–501 (2010).
405 46. Afonine, P. V. *et al.* Real-space refinement in PHENIX for cryo-EM and
406 crystallography. *Acta Crystallogr D Struct Biol* **74**, 531–544 (2018).
407 47. Liebschner, D. *et al.* Macromolecular structure determination using X-rays,

408 neutrons and electrons: recent developments in Phenix. *Acta Crystallogr D Struct*
409 *Biol* **75**, 861–877 (2019).
410 48. Pintilie, G. *et al.* Measurement of atom resolvability in cryo-EM maps with Q-
411 scores. *Nat Methods* **17**, 328–334 (2020).
412 49. Yamashita, K., Palmer, C. M., Burnley, T. & Murshudov, G. N. Cryo-EM single-
413 particle structure refinement and map calculation using Servalcat. *Acta Crystallogr*
414 *D Struct Biol* **77**, 1282–1291 (2021).
415 50. Pettersen, E. F. *et al.* UCSF ChimeraX: Structure visualization for researchers,
416 educators, and developers. *Protein Science* **30**, 70–82 (2021).
417

418 **Figure legends**

419 **Fig. 1 Structure of the twin motor featuring dimeric F_1-like ATPase.**

420 (**a**) Gliding machinery of *Mycoplasma mobile*. Overall view of the gliding machinery
421 (top) and part of the internal chain (bottom). (**b**) Overall structure of the twin motor. The
422 illustration is drawn in the upper left. Scale bar = 25 Å. (**c**) Atomic model of the twin
423 motor. Black triangles represent nucleotides. Maps in (b) and (c) are contoured at 0.55
424 in UCSF ChimeraX. (**d**) Dimeric F_1-like ATPase in the twin motor. Dotted lines indicate
425 the axis of each ATPase. (**e**) Density of Mg-ATP bound to F_1-like ATPase. The dotted
426 region in (c) is shown. (**f, h, j**) Subunits constituting F_1-like ATPase. (**g, i, k**) Overlay of
427 subunits of F_1-like ATPase and *Bacillus* PS3 F_1-ATPase. The subunits of the *Bacillus*
428 PS3 F_1-ATPase, αβ (PDB ID: 8HH5) and γ (PDB ID: 8HH2), are coloured purple.
429

430 **Fig. 2 Interaction between subunits.**

431 (**a**) N- and C-terminal regions of the twin motor. The twin motor is viewed from the top

of the illustration. Arrows indicate the interface between dimeric F_1-like ATPases. Maps are contoured at 0.55 in UCSF ChimeraX. (**b**) Structure of Gliβ and PGK. (**c**) Interaction between the N-terminal region of Gliβ and Gliα-NBD at the interface between dimeric F_1-like ATPases. The dotted region in (a) is shown. (**d**) Interaction of PGK with the Gliβ-NTD. The dotted region in (a) is shown. (**e**) Structure of the Gliα and GliD monomers. (**f**) GliD dimer at the interface between dimeric F_1-like ATPases. The figure corresponds to the dotted region in the illustration. (**g, h**) Interaction between GliD and Gliα-CTD. Each corresponds to the dotted regions in (f).

Fig. 3 Structural conformations and nucleotide binding of Gliβ.

(**a**) Differences in the conformations of the three Gliβ. Superposed three Gliβs in the F_1-like ATPase. The dotted lines indicate the position of the DELSEED loop of each Gliβ. (**b**) Nucleotide binding pattern of dimeric F_1-like ATPase and F_1-ATPase. The catalytic site is circled by black dotted lines. (**c**) Gliαβ dimer in each conformation in the hexamer. (**d**) Comparison of the catalytic sites. Each catalytic site corresponds to the dot square above. The catalytic sites are superimposed on the corresponding catalytic sites of F_1-ATPase (PDB ID: 8HHA), which are coloured purple.

Fig. 4 Structure and motion of the gliding machinery.

(**a**) Fitting of the atomic model of the twin-motor into the EM map of the motor chain. The right panel indicates the interface between GliDs. (**b**) Possible rotational catalytic mechanism of F_1-like ATPase. Gliγ is indicated by yellow arrows, the direction of which indicates the conformational tilt. (**c**) A possible explanation for the conversion mechanism from rotational to linear motion. Dotted arrows indicate unknown force

transduction in the cell membrane. Gli349 and Gli521 are depicted in red and green, respectively. Unidentified protein regions in the gliding machinery are coloured purple.

Methods

Optical microscopy

The cells of the *M. mobile* mutant strain (gli521 [P476R]), which can glide like the wild type strain but binds sialylated oligosaccharides more tightly, were cultured, observed using phase-contrast microscopy, and recorded as previously described[32–35]. The recorded video was analysed using ImageJ software v1.54d (https://imagej.nih.gov/ij/).

Isolation of the twin motor

The twin motor was isolated from the *M. mobile* mutant strain (gli521 [P476R]), as previously described[2]. The twin motor sample with phosphate-buffered saline (PBS) consisting of 8.1 mM Na_2HPO_4, 1.5 mM KH_2PO_4 (pH 7.3), 2.7 mM KCl and 137 mM NaCl, and 1 mM $MgCl_2$ was concentrated to 1 mg/mL using a 100K Vivaspin concentrator (Merck, Germany) with 0.1% (w/v) CHAPS to prevent membrane adsorption. The concentrated twin-motor was subjected to 12.5% SDS-PAGE and stained using Coomassie brilliant blue R-250. The bands of the component proteins were identified using peptide mass fingerprinting, as previously described[36].

Cryo-EM grid preparation and data acquisition

An EG-grid was prepared as previously described[37]. A 2.6 μL sample solution was applied on the grid, automatically blotted from both sides with filter paper at 4 °C for 2 s at 100% humidity, and vitrificated using the semi-automated vitrification device,

480 Vitrobot Mark IV (Thermo Fisher Scientific, USA). Cryo-EM imaging was performed
481 using a CRYO ARM 300 (JEOL, Japan) operated at 300 kV with a K3 direct electron
482 detector camera (AMETEK, Gatan, USA). A total of 7,350 movies were recorded using
483 SerialEM software[38] with a total dose of approximately 80 electrons $Å^{-2}$ for 40 frames,
484 an exposure time of 3.3 s per movie, and a nominal defocus range of -0.8 to -1.8 μm.
485 The nominal magnification was 60,000×, corresponding to 0.87 Å per pixel.
486

487 **Cryo-EM image processing**

488 The image processing steps for SPA are summarised in Extended Data Figs. 3 and 4.
489 Image processing was performed using cryoSPARC v3.3.2[39], unless otherwise stated.
490 Movies were aligned using patch-based motion correction, and the contrast transfer
491 function (CTF) parameters were estimated using patch CTF estimation. Micrographs
492 with a CTF fit resolution worse than 8 Å were removed. Particles were automatically
493 picked up using a Blob Picker, extracted with ×4 binning, and 2D-classified. The
494 obtained 2D averaged images were used as templates for the Template Picker to pick up
495 good particles. After two rounds of 2D classification, the selected good particles were
496 subjected to local motion correction and re-extracted with the original pixel size. The
497 particles were subjected to Ab-initio reconstruction using C1 symmetry enforced with a
498 final resolution limit of 12 Å and heterogeneous reconstruction with 3 classes. Particles
499 in class 2 were subjected to homogeneous reconstruction using C1 symmetry, resulting
500 in a map at a resolution of 3.5 Å. The final map was generated via local and global CTF
501 refinement, and then non-uniform refinement. To improve the local resolution, the final
502 map and particles were subjected to particle subtraction and local refinement using C1
503 symmetry to generate half-divided maps, each containing a monomeric ATPase. The

504 whole and two local maps were subjected to mask creation and postprocessing in
505 RELION 4.0[40], resulting in resolutions of 3.2, 3.1, and 3.1 Å, respectively. Local
506 resolution estimation was also performed in RELION 4.0. The post-processed map was
507 denoised using Topaz software v0.2.5 with the trained model Unet-3d-10a[41]. RELION
508 4.0 was used to calculate the Fourier shell correlation (FSC) curve between two half-
509 maps and estimate the local resolution.
510
511 **Modelling**
512 Initial models for GliαβγDE were generated using AlphaFold2[42], whereas the homology
513 model for PGK was generated using Modeller v10.4[43] with the atomic model of PGK
514 (PDB ID: 4DG5) from *S. aureus*. The generated models were fitted to the corresponding
515 densities of the EM map as rigid bodies using UCSF Chimera v1.15[44]. The fitted models
516 were manually inspected and adjusted using COOT v0.9.8.1[45] and refined using the
517 *phenix.real_space_refine* program in PHENIX v1.19[46,47] with reference model restraints
518 using atomic models of F_1-ATPase (PDB ID: 5IK2) from *Caldalaklibacillus thermarum*
519 and PGK (PDB ID: 3ZLB) from *Streptococcus pneumoniae*. Manual adjustment using
520 COOT and refinement using PHENIX were repeated until model parameters were no
521 longer improved. FSC curves between the map and model were calculated using
522 PHENIX. The refined model was also evaluated via comprehensive validation in
523 PHENIX and the Q-score[48]. To identify the nucleotide binding sites of F_1-like ATPases,
524 F_o-F_c maps were generated using Servalcat[49]. Superposition of models and fitting of
525 models to the map were performed using UCSF ChimeraX v1.2.5[50]. All structural
526 figures were obtained using UCSF ChimeraX.
527

Data availability

The cryo-EM map for the twin motor is available on the Electron Microscopy Data Bank (EMDB) under accession code: EMD-60718. The coordinates have been deposited in the Protein Data Bank (PDB) under accession code: 9IO5.

Acknowledgments

We thank Tomomi Shimonaka at Osaka Metropolitan University and Fumiaki Makino at Osaka University for their technical assistance. This manuscript was edited using Copilot, an AI tool. This study was supported by Grants-in-Aid for Scientific Research (A) (JP17H01544), a JST CREST grant (JPMJCR19S5) to M.M., and Research Support Project for Life Science and Drug Discovery (BINDS) from AMED under Grant Number, JP22am121003, to K.N., and JEOL YOKOGUSHI Research Alliance Laboratories of Osaka University to K.N.

Author contributions

T.T. and M.M. conceived the strategy. M.M. and K.N. supervised the research. T.T. prepared the cryo-EM samples and carried out the biochemical analyses. J.F. prepared EG-grid for cryo-EM observation. A.K. and T.M. performed cryo-EM. T.T. carried out 3D reconstruction and model building. T.K., T.H., A.K., T.M., K.K., and K.N. participated in the discussion regarding the structural analyses. T.T. and M.M. wrote the manuscript with input from all authors.

Competing interests

The authors have declared no competing interest.

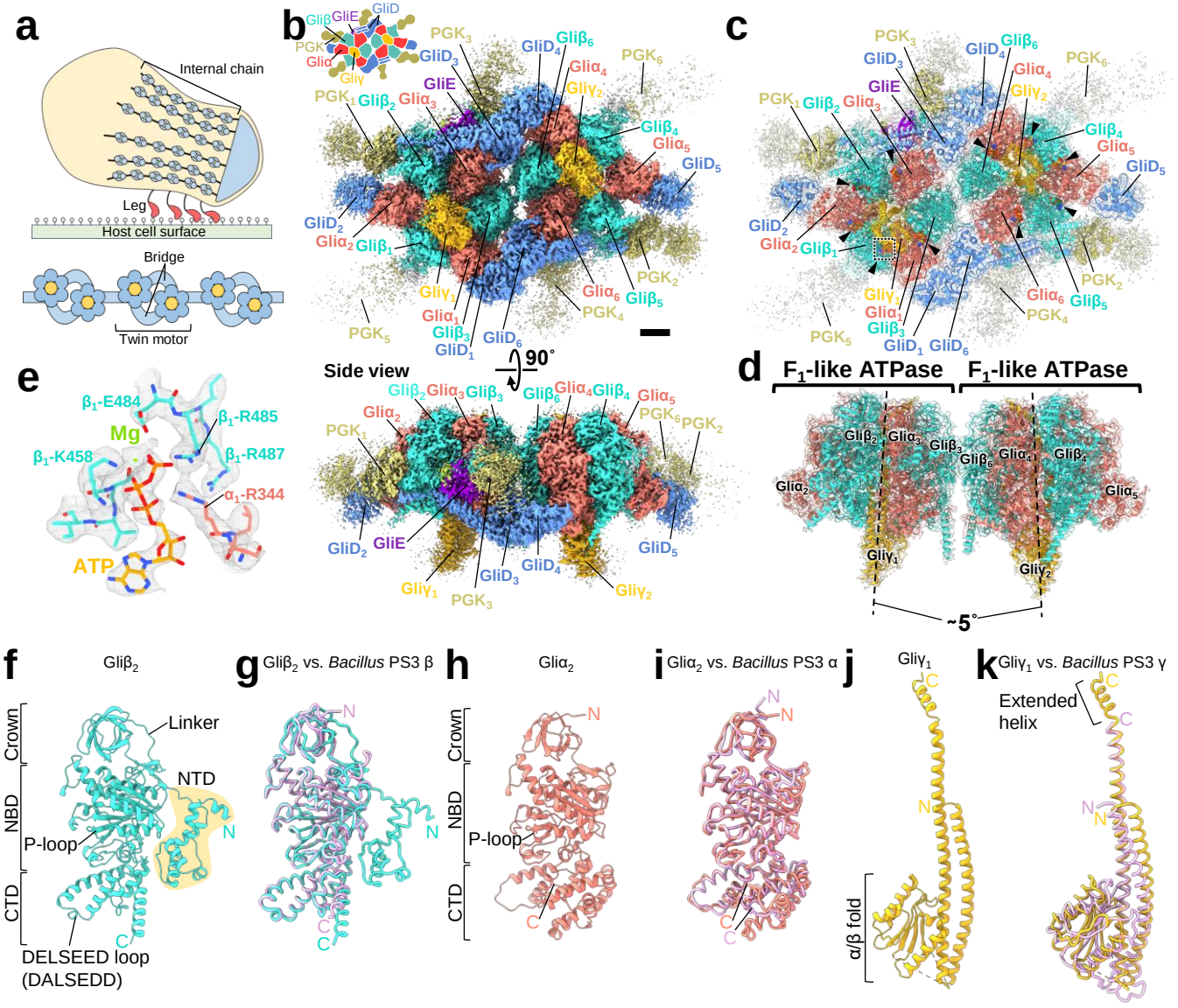
a
Internal chain
Leg
Host cell surface
Bridge
Twin motor
b
c
Side view
90°
d
F1-like ATPase
F1-like ATPase
~5°
e
β1-E484
β1-R485
Mg
β1-K458
β1-R487
α1-R344
ATP
f
Gliβ2
Linker
NTD
Crown
NBD
CTD
P-loop
DELSEED loop
(DALSEDD)
g
Gliβ2 vs. Bacillus PS3 β
h
Gliα2
i
Gliα2 vs. Bacillus PS3 α
j
Gliγ1
α/β fold
k
Gliγ1 vs. Bacillus PS3 γ
Extended
helix

Fig. 1

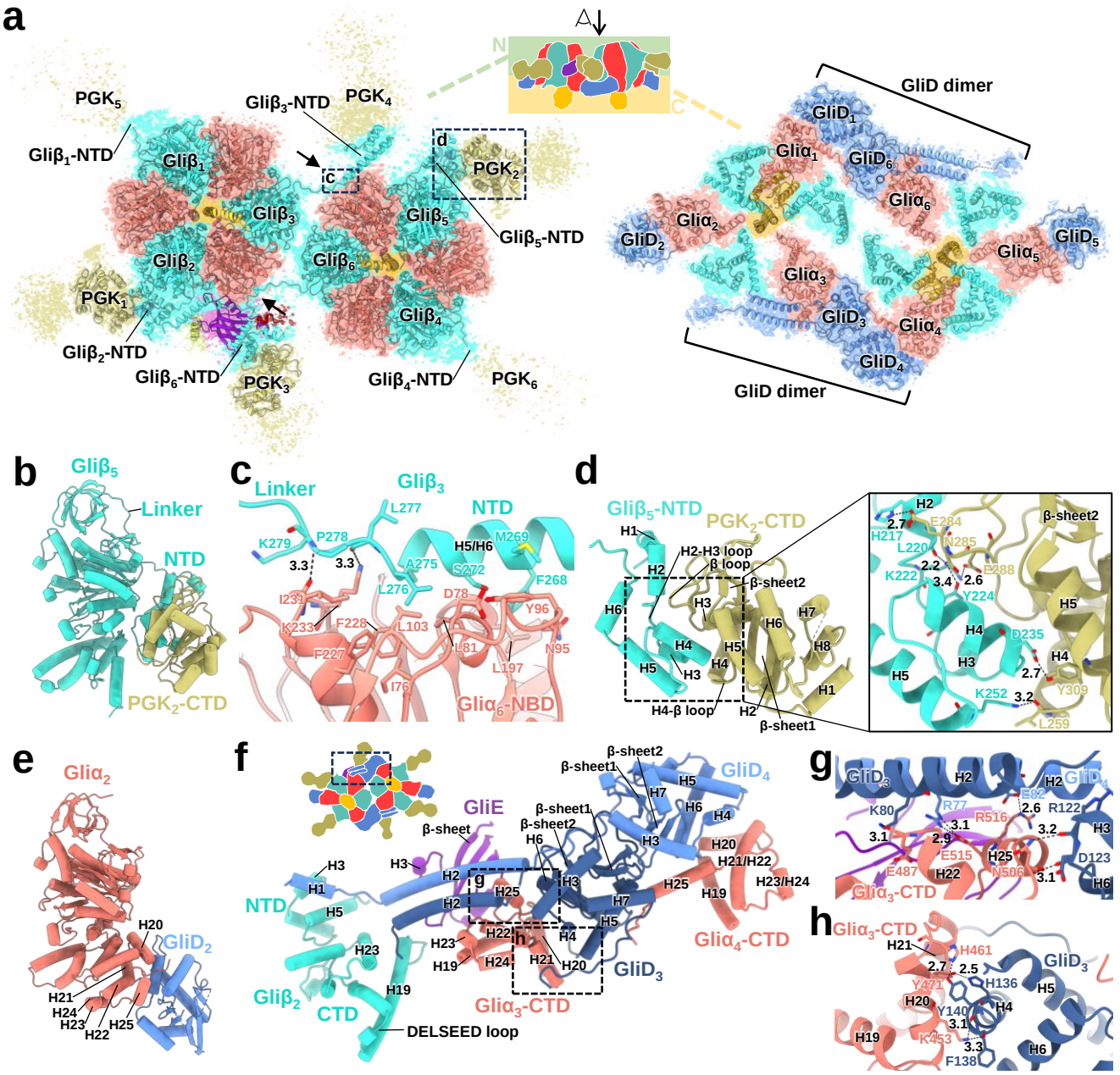
a
A
N
C
PGK5
Gliβ1-NTD
Gliβ1
Gliβ3-NTD
PGK4
c
d
PGK2
Gliβ3
Gliβ5
Gliβ5-NTD
Gliβ2
Gliβ6
PGK1
Gliβ2-NTD
Gliβ6-NTD
PGK3
Gliβ4
Gliβ4-NTD
PGK6
GliD dimer
GliD1
Gliα1
GliD6
Gliα6
Gliα2
GliD2
Gliα5
GliD5
Gliα3
GliD3
Gliα4
GliD4
GliD dimer
b
Gliβ5
Linker
NTD
PGK2-CTD
c
Linker
Gliβ3
NTD
L277
K279
P278
3.3
3.3
H5/H6
M269
A275
S272
F268
L276
D78
I233
Y96
K233
F228
L103
N95
F227
L81
L197
I76
Gliα6-NBD
d
Gliβ5-NTD
PGK2-CTD
H1
H2-H3 loop
β loop
H2
β-sheet2
H3
H6
H7
H6
H4
H5
H8
H5
H3
H4
H1
H4-β loop
H2
β-sheet1
H2
2.7
E284
β-sheet2
H217
L220
N285
2.2
E288
K222
3.4
2.6
Y224
H5
H4
D235
H3
H4
2.7
H5
K252
3.2
Y309
L259
e
Gliα2
H20
GliD2
H21
H24
H23
H22
H25
f
β-sheet2
β-sheet1
GliD4
H5
H7
H6
H4
GliE
β-sheet1
β-sheet2
β-sheet
H6
H3
H20
H21/H22
H3
H3
H2
g
H25
H3
H25
H23/H24
H19
NTD
H1
H2
H7
H5
H5
H22
h
H4
H23
H23
H24
H21
H20
H19
GliD3
Gliα4-CTD
Gliβ2
CTD
H19
Gliα3-CTD
DELSEED loop
g
GliD3
H2
H2
GliD4
E82
K80
R77
R516
2.6
R122
3.1
3.1
3.2
H3
2.9
E515
H25
D123
E487
H22
N506
3.1
H6
Gliα3-CTD
h
Gliα3-CTD
H21
H461
2.7
2.5
GliD3
Y471
H136
H5
H20
Y140
H4
3.1
H19
K453
3.3
H6
F138

Fig. 2

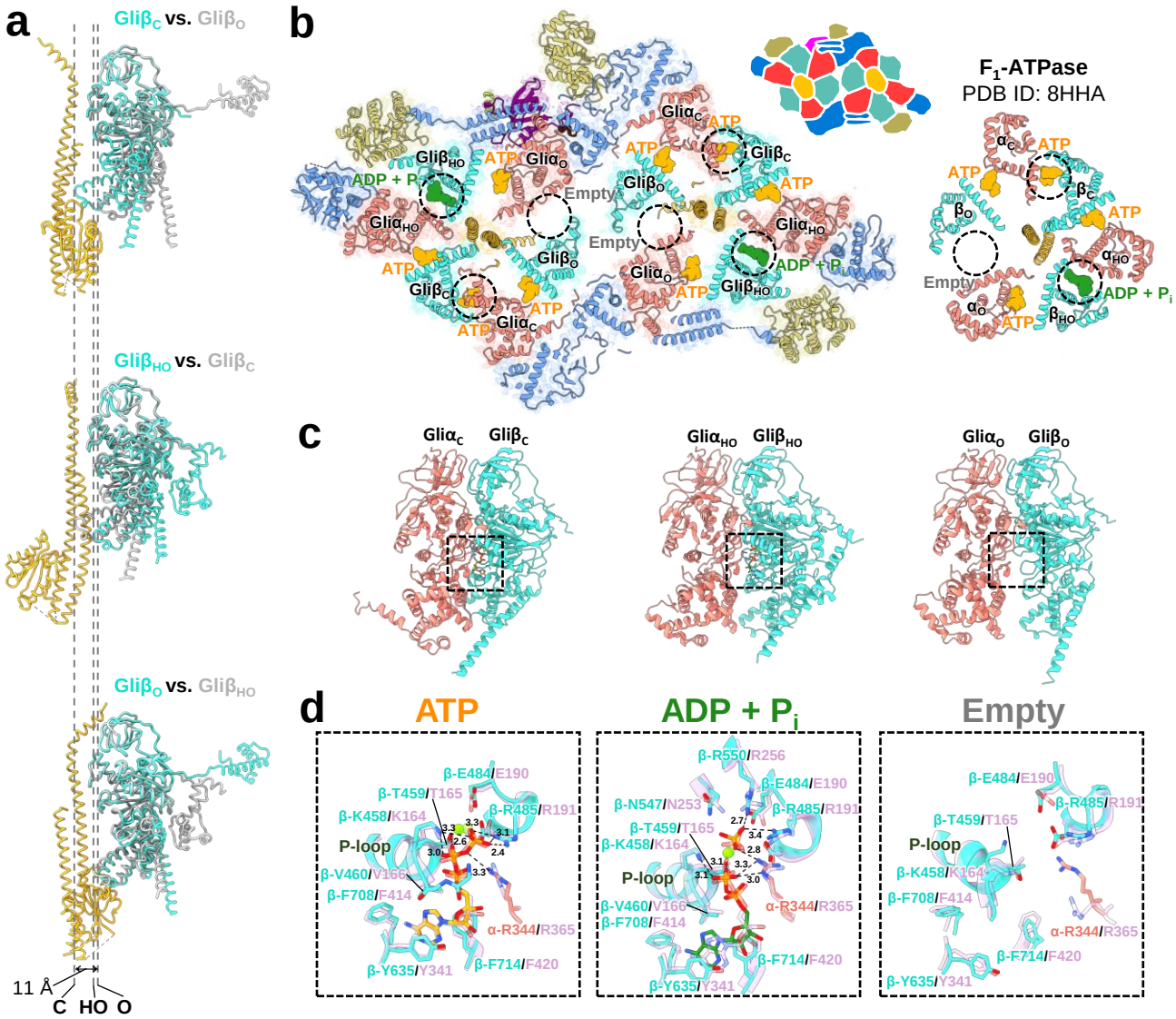
a
Gliβ$_C$ vs. Gliβ$_O$
Gliβ$_{HO}$ vs. Gliβ$_C$
Gliβ$_O$ vs. Gliβ$_{HO}$
11 Å
C HO O
b
F$_1$-ATPase
PDB ID: 8HHA
ADP + P$_i$
ATP
Empty
c
Gliα$_C$ Gliβ$_C$
Gliα$_{HO}$ Gliβ$_{HO}$
Gliα$_O$ Gliβ$_O$
d
ATP
ADP + P$_i$
Empty
P-loop
β-E484/E190
β-T459/T165
β-K458/K164
β-R485/R191
β-V460/V166
β-F708/F414
α-R344/R365
β-F714/F420
β-Y635/Y341
β-R550/R256
β-N547/N253

Fig. 3

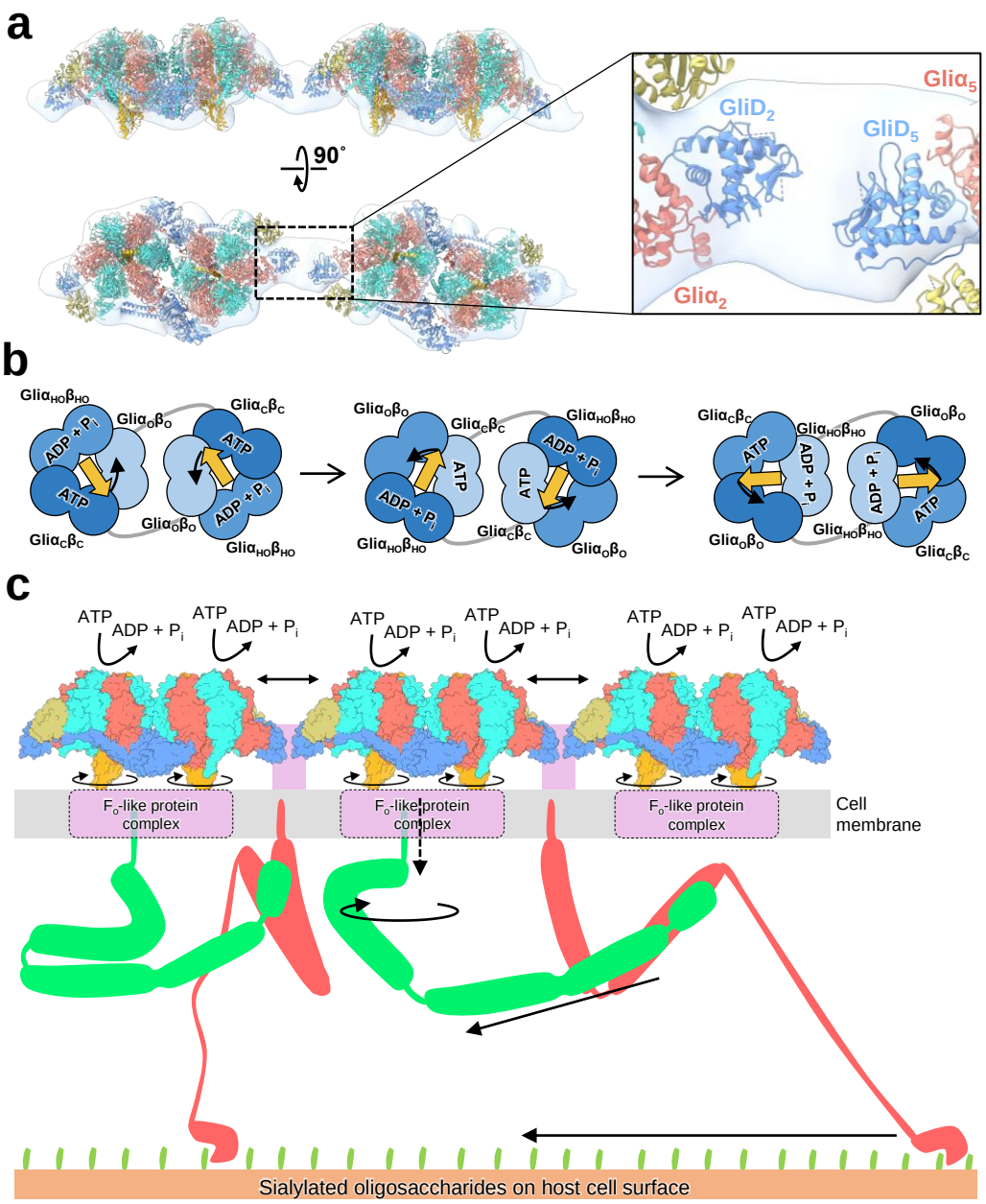
a
90˚
Gliα5
GliD2
GliD5
Gliα2
b
GliαHOβHO
GliαOβO
GliαCβC
ADP + Pi
ATP
c
ATP
ADP + Pi
Fo-like protein complex
Cell membrane
Sialylated oligosaccharides on host cell surface

Fig. 4